Quarterly Journal of the Royal Meteorological Society Q. J. R. Meteorol. Soc. 141: 714–726, April 2015 A DOI:10.1002/qj.2383

RMetS
Royal Meteorological Society

Tropical cyclone convection: the effects of a vortex boundary-layer wind profile on deep convection

Gerard Kilroy* and Roger K. Smith
Meteorological Institute, Ludwig-Maximilians University of Munich, Germany

*Correspondence to: G. Kilroy, Meteorological Institute, Ludwig-Maximilians University of Munich, Theresienstr. 37, 80333 Munich, Germany. E-mail: gerard.kilroy@lmu.de

We describe idealized numerical model experiments to study the effects of a vortex boundary-layer wind profile on the generation of vertical vorticity in tropical deep convection. Situations are considered in which there is either no vertical shear above the boundary layer or negative vertical shear appropriate to a warm-cored vortex. Deep convection growing in these environments develops dipole structures of vertical vorticity in which the cyclonic gyre is favoured and persists longer than the anticyclonic one. The orientation of the dipole at a particular height is determined partly by that of the ambient horizontal vortex lines, which rotate with height, and also by the vertical advection of vertical vorticity from below.

An increase in the magnitude of boundary-layer shear enhances the distortion of the initial thermal, weakening its subsequent ascent rate. This effect is detrimental to vertical vorticity production by stretching but, because the increase in shear implies an increase in the magnitude of horizontal vorticity that can be tilted, its net effect on the vertical vorticity production by tilting cannot be foreseen. In the calculations described, the effect of the increased horizontal vorticity dominates, so that updraughts rising in stronger vertical shear have larger vertical vorticity maxima, despite smaller vertical velocity maxima.

With negative vertical shear above the boundary layer, the vorticity dipole reverses in sign with height, as in a recent study of the effects of unidirectional shear. The results provide a basis for appraising a recently proposed conceptual model for the inward contraction of eyewall convection in tropical cyclones, as well as a starting point for developing an improved understanding of the formation of a vorticity monopole during tropical cyclogenesis.

Key Words: tropical cyclones; rotating deep convection; vortical hot towers

Received 21 October 2013; Revised 26 February 2014; Accepted 5 April 2014; Published online in Wiley Online Library 24 June 2014

1. Introduction

In a recent article (Kilroy *et al.*, 2014; henceforth KSW), we described a series of numerical model experiments designed to investigate aspects of deep convection in tropical depressions, including the effects of a *unidirectional* boundary-layer wind structure on storm structure, especially on vertical vorticity production and updraught splitting. We investigated also the combined effects of horizontal and vertical shear on vertical vorticity production, with and without background rotation. We noted *inter alia* that, in the classical middle-latitude thunderstorm environment, the wind increases in strength with height, so that the local crosswise vorticity has a single sign (see Ramsay and Doswell, 2005, their figure 1). However, in tropical depressions and tropical cyclones, the tangential wind speed decreases with height above a shallow boundary layer so that the sign of the radial vorticity component changes sign at some low level, typically on the order of a few kilometres. It was shown that the tilting of horizontal vorticity by a convective updraught leads not only to dipole patterns of vertical vorticity, but also to a reversal in sign of the vorticity with height. These findings add a layer of complexity to interpretations of the aggregation of convectively induced cyclonic vorticity anomalies in terms of barotropic dynamics (e.g. Nguyen *et al.*, 2008). In fact, in a theoretical study of tropical cyclogenesis in a moist Boussinesq model, Deng *et al.* (2012) pointed out that, for strong, unidirectional, low-altitude shear, the convective updraughts have a low altitude vorticity dipole rather than a cyclonic monopole, making them less conducive to the formation of a larger-scale cyclonic vortex.

A further complication in the context of tropical cyclones is that there is a significant radial wind component in the boundary layer, an effect that was omitted in the foregoing studies. This wind component may increase or decrease with height at low levels, depending on the radius (see e.g. Smith and Montgomery, 2013). Thus, the unidirectional vertical wind profiles examined in KSW may be overly simplistic when applied to tropical cyclones. For this reason, we report here the results of a series of numerical experiments to examine the additional effects of a typical radial

wind profile in a tropical cyclone on the structural evolution of vertical vorticity in deep convection. We see these experiments as a necessary first step to developing an improved understanding of the aggregation of convectively induced cyclonic vorticity anomalies in developing tropical cyclones.

While there have been several numerical studies of convective cells developing in environments where the wind hodograph turns with height (e.g. Klemp and Wilhelmson, 1978; Schlesinger, 1978; Weisman and Klemp, 1984), to our knowledge, none of these have examined a typical vortex boundary-layer-type wind profile. Klemp and Wilhelmson (1978) showed that if the wind hodograph turns clockwise with height, the right-moving storm is favoured, whereas an anticlockwise-turning hodograph favours the development of the left-moving cell. Rotunno (1981) and Rotunno and Klemp (1982) provided an explanation for this behaviour based on linear theory, which predicts that, for a clockwise turning hodograph, the interaction of the mean shear with the updraught produces an upward-directed perturbation pressure gradient on the right flank of the updraught and a downward-directed perturbation pressure gradient on the left flank. These pressure gradients lead to subsequent development of the updraught on the right flank. Their analyses suggest that, although nonlinear effects strongly promote splitting of the updraught, the linear forcing remains the dominant factor in preferentially enhancing updraught growth on one flank.

In a recent article, Hogsett and Stewart (2014) proposed an interesting conceptual model involving storm splitting to explain the inward contraction of eyewall convection in tropical cyclones. The model is based on the idea that deep convection growing in the rapidly rotating environment of a tropical cyclone might have a character similar to 'supercell convection', which in the middle latitudes is a by-product of storm splitting. Exploiting the analogy with splitting storms in the middle latitudes, they likened the radially inward movement of the cyclonic cell of a split pair to the cyclonic 'right mover' of a split pair in the middle latitudes. They noted that, because the vertical shear of the tangential wind is negative in the tropical cyclone, the cyclonic cell of a pair occurs to the left of the azimuthal mean (tangential) wind (i.e. radially inwards) and referred to this cell as a 'left mover'. They argued that the anticyclonic cell to the right of the mean tangential wind would be weakened by the production of cyclonic vertical vorticity by stretching in the updraught of this cell. We believe the idea is worthy of further investigation, especially in view of the potentially modifying role of ambient horizontal vorticity associated with the positive vertical shear in the boundary layer and the shear associated with the radial wind component.

This article presents the results of our extended numerical modelling study referred to above, as well as an appraisal of the Hogsett and Stewart conjecture. The article is organized as follows. In section 2 we give a brief description of the numerical model and the configuration of the experiments is described in section 3. The results are presented in sections 4–8 and an appraisal of the Hogsett and Stewart conjecture is given in section 9. Conclusions are given in section 10.

2. The numerical model

The numerical model used for this study is the state-of-the-art three-dimensional cloud model of Bryan and Fritsch (2002) and Bryan (2002). The reader is referred to section 2 of KSW for further details. The present experiments use the same model configurations as those of Experiments 2, 3 and 8 of Wissmeier and Smith (2011), except that the horizontal grid spacing is halved to give improved horizontal resolution of the cloud updraughts. The horizontal domain size is 50 km × 50 km with a uniform horizontal grid spacing of 250 m. The vertical domain extends to a height of 28 km, with the vertical grid interval stretching smoothly from 120 m at the surface to 1000 m at the top. There are 50 grid levels in the vertical, eight of which are below 1.5 km. The large time step is 3.7 s and the integration time is 2 h. There are eight small time steps per large time step to resolve fast-moving sound waves. The default 'open' boundary conditions are used at the lateral boundaries (Durran and Klemp, 1983). For simplicity, radiation effects are neglected and there are no surface fluxes of momentum, heat and moisture. A sponge layer is implemented in the uppermost 2 km to inhibit the reflection of gravity waves from the upper boundary. All experiments include warm rain physics only. The subgrid turbulence scheme used is the Smagorinsky large-eddy simulation scheme (Smagorinsky, 1963). As in Wissmeier and Smith (2011), the calculations are not initialized from a geostrophically balanced state because the Bryan model is not easily configured to allow this and also because interest is confined to times much shorter than the inertial period (on the order of 6 h).

Table 1. Details of the seven experiments studied herein. The Coriolis parameter, f, has the value $\zeta_o = 3 \times 10^{-4} s^{-1}$. All experiments are initiated with a 3 K thermal perturbation. The wind profiles are discussed further in section 3.1.

Exp	f	BL profile	Above BL	Ref wind ($m\,s^{-1}$)
1	0	Standard	No shear	10
2	0	Standard	Neg shear	10
3	0	Standard	No shear	5
4	0	Standard	No shear	15
5	ζ_o	Standard	No shear	10
6	ζ_o	Gale force	No shear	17
7	ζ_o	Gale force	Neg shear	17

3. The numerical experiments

We describe seven numerical experiments, details of which are summarized and compared in Table 1. Further details of the experiments and their purpose are given in the appropriate sections.

3.1. *Background wind profiles*

The ambient vertical wind profiles $(U(z), V(z))$ used in all the experiments reported here have the qualitative structure of a turbulent vortex boundary layer and are shown in Figure 1. The profiles are obtained from the linear vortex boundary-layer solution of Vogl and Smith (2009), which satisfies a surface drag law on the wind field. In this solution, $U(z)$ and $V(z)$ are the radial and tangential wind components. When expressed in a rectangular coordinate system (x, y, z), where z is the height, the profiles have the form:

$$U(z) = -V_a \exp(-Z_a)\,[A_1 \sin Z_a + A_2 \cos Z_a]\,, \qquad (1)$$

$$V(z) = V_a\,(1 - \exp(-Z_a))\,[B_1 \cos Z_a - B_2 \sin Z_a]\,, \qquad (2)$$

where A_1, A_2, B_1, B_2 are constants, $Z_a = z/Z_g$ is a non-dimensional height, Z_g is the boundary-layer depth scale and V_a is the (tangential) wind speed at the top of the boundary layer.

The profile for Experiments 1-5 has parameters $A_1 = 0.356$, $A_2 = 0.192$, $B_1 = A_1$, $B_2 = A_2$, $Z_g = 632$ m, with V_a given in Table 1. In Experiment 2, a wind profile with unidirectional, negative vertical shear is blended with the above profile above a height of 2 km so that $V(z)$ decreases with height. The equation for $V(z)$ above 2 km is given in KSW and was used in their Experiments 1–3. The low-level wind profile for Experiments 6 and 7 is characteristic of the region of gales in a tropical cyclone and has parameters $A_1 = -0.415$, $A_2 = 0.202$, $B_1 = -0.304$, $B_2 = -0.625$, $Z_g = 472$ m and $V_a = 17\,m\,s^{-1}$. In Experiment 6, there is a uniform flow with gale-force strength ($17\,m\,s^{-1}$) above 2 km, while Experiment 7 has a profile with unidirectional negative shear, similar to Experiment 2.

Figure 2 shows the non-dimensional wind hodograph for the wind profiles described above. The surface wind is non-zero

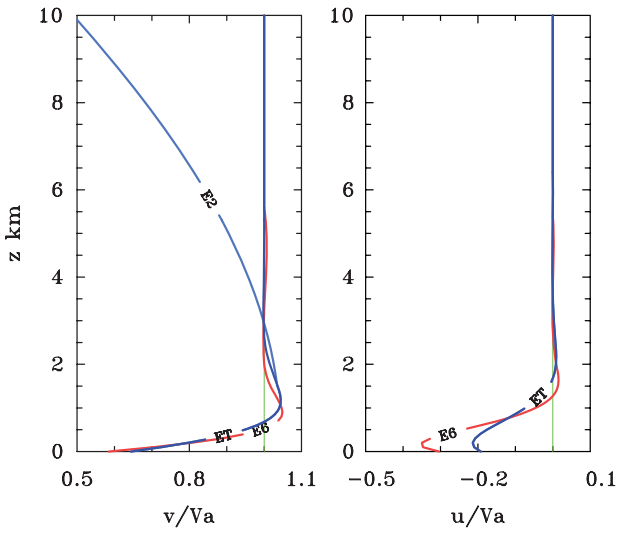

Figure 1. The background wind flow used for all experiments. The left profile (a) denotes the non-dimensional V component and the right profile (b) denotes the non-dimensional U component for the wind profiles in Experiments 1 and 3–5 (blue contour labelled ET), Experiment 2 (light blue contour labelled E2) and Experiment 6 (red contour labelled E6). Experiment 7 combines the boundary-layer profile used in Experiment 6 and the upper-level negative shear profile used in Experiment 2. These profiles are multiplied by the reference wind value given in Table 1 for each experiment.

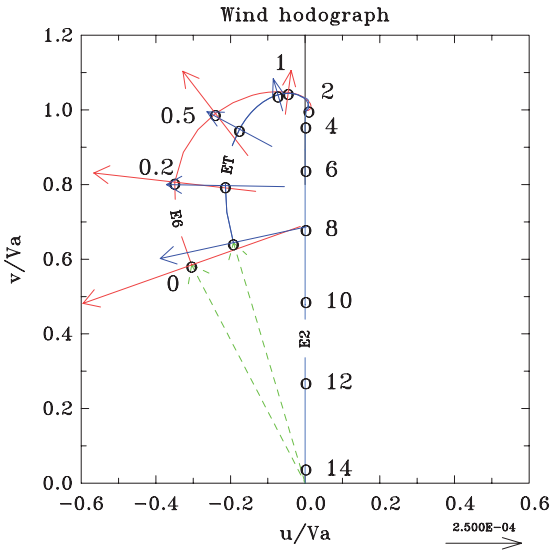

Figure 2. The background wind hodograph for the non-dimensional wind profiles in Experiments 1 and 3–5 (blue contour labelled ET) and Experiment 6 (red contour labelled E6). The light blue (labelled E2) line represents the uni-directional vertical wind shear for heights above 2 km in Experiment 2. This experiment has the same wind profile as Experiments 1 and 3–5 below a height of 2 km. Experiment 7 combines the boundary-layer profile used in Experiment 6 and the upper-level negative shear profile used in Experiment 2. The circular marks and accompanying numbers represent heights. The arrows normal to the curves labelled ET and E6 show the direction and relative magnitude of the horizontal vorticity at those heights. The thin dashed (green) lines represent the wind vectors at the surface. A reference vector for the magnitude of the horizontal vorticity is given at the bottom right of the plot.

and typically about 0.6 times that at a height of 2 km. Above a height of 2 km, $V(z)$ is approximately constant, equal to V_a, in Experiments 1 and 3–6, while in Experiments 2 and 7 it decays linearly with height. In all experiments, $U(z) \to 0$ above this height. The magnitude and orientation of the horizontal vorticity are indicated in Figure 2 by arrows normal to the wind curves at the surface and at heights of 200 m, 500 m and 1 km. Below a height of 2 km, the magnitude of horizontal vorticity is larger in the wind profile used in Experiments 6 and 7 than that used in Experiments 1–5, while above this height there is practically no horizontal vorticity, except in Experiments 2 and 7.

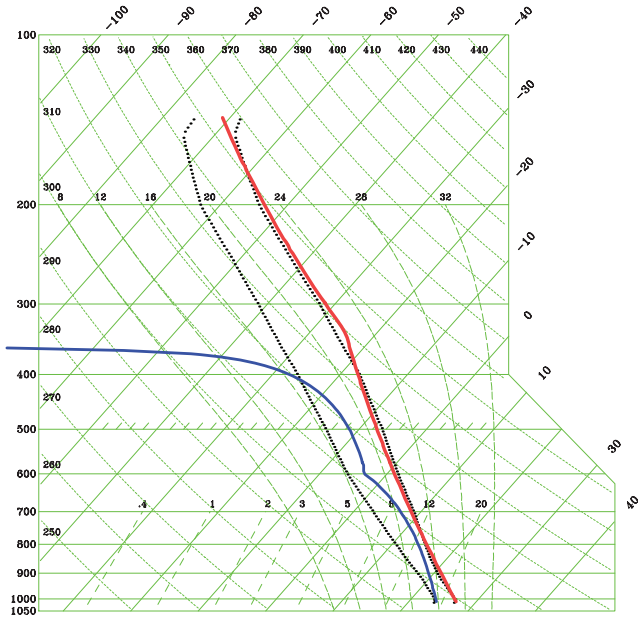

Figure 3. Skew-T–log p diagram showing the temperature (right solid curve) and dew-point temperature (left solid curve) of the sounding used in this study. For comparison, the dotted curves show the temperature (right curve) and dew-point temperature (left curve) for the mean tropical sounding of Dunion and Marron (2008).

A uniform flow is added to the wind profile in all experiments in order to keep the convection near the centre of the computational domain. The value of this flow is determined by trial and error and is different for each experiment.

3.2. *Representation of vertical vorticity*

The calculation in Experiments 5–7 are carried out on an f-plane with the Coriolis parameter $f = \zeta_o$, where $\zeta_o = 3 \times 10^{-4}\,\mathrm{s}^{-1}$, a value typical of that in a tropical depression.* The use of an f-plane with an enhanced value of f beyond a typical tropical value is a simple expedient to model the background rotation of the vortex in the present problem.

3.3. *Thermodynamic sounding*

All experiments use the idealized thermodynamic sounding shown in Figure 3. This sounding is the 'standard' sounding used in KSW, which has piecewise-linear profiles of virtual potential temperature θ_v and mixing ratio r. The Convective Available Potential Energy (CAPE) is $2080\,\mathrm{J\,kg^{-1}}$. The construction of this sounding is based on an observed sounding made near the centre of the low-level circulation of ex-Tropical Storm *Gaston* during the Pre-Depression Investigation of Cloud-systems in the Tropics (PREDICT) experiment (see Smith and Montgomery, 2012, their figure 6). This region of ex-*Gaston* was one of high total precipitable water (TPW), high CAPE and low Convective Inhibition (CIN). This sounding has a minimum CIN of $40\,\mathrm{J\,kg^{-1}}$ and a TPW value of $59.1\,\mathrm{kg\,m^{-2}}$. The calculation of the foregoing values of CAPE and CIN is described in KSW. The value of CAPE used in the study ($2080\,\mathrm{J\,kg^{-1}}$) is typical of that found in a tropical depression environment (Smith and Montgomery, 2012) and similar also to the values used in previous studies of convection in idealized shear profiles (Wilhelmson and Klemp, 1978; Weisman and Klemp, 1984; Rozoff, 2007), but is roughly twice that found in a study by Molinari and Vollaro (2010) of the inner 400 km region of tropical cyclones sampled during the Convection and Moisture Experiments (CAMEX).

*See Foster and Lyons, 1984; Wissmeier and Smith, 2011, section 2.3.

3.4. Initiation of convection

Convection is initiated by a symmetric thermal perturbation with a horizontal radius of 5 km and a vertical extent of 1 km, as in KSW and in Kilroy and Smith (2012). The temperature excess has a maximum at the surface at the centre of the perturbation and decreases monotonically to zero at the perturbation's edge. The perturbation centre coincides with the centre of the domain. In general, the details of the ensuing convection such as the updraught depth and the maximum updraught strength will depend on the amplitude and spatial structure of the thermal perturbation. A maximum temperature perturbation of 3 K is used in all experiments, which is 1 K larger than that used in Kilroy and Smith (2012) and in KSW. The larger thermal perturbation used here is due to the fact that the low-level vertical wind shear in these experiments completely suppresses convection with a thermal perturbation of only 2 K.

3.5. The experiments in brief

Experiment 1 is designed to isolate the effects of a vortex boundary layer shear profile and serves as a control experiment. It has a background reference wind of $10\,\mathrm{m\,s^{-1}}$ and no background rotation (Table 1). A detailed analysis of this experiment is carried out in the next section. Experiment 2 is similar to Experiment 1, but above 2 km it has a unidirectional vertical wind profile with negative vertical shear, making it more realistic *vis-á-vis* a tropical warm-cored vortex. Experiments 3 and 4 are similar to Experiment 1, but a value V_a that is half or 1.5 times that in Experiment 1, respectively, giving smaller or larger low-level wind shear. These experiments are designed to examine the dependence of the ensuing convection on the magnitude of the low-level wind shear.

Experiment 5 is a repeat of Experiment 1 with background vertical vorticity typical of that in a tropical depression. Finally, Experiments 6 and 7 are repeats of Experiments 1 and 2 but have a 70 % stronger wind speed at a height of 2 km and a stronger transverse (radial) flow near the surface (cf. Figure 1(b)), making the wind profile more typical of that in the region of gales in a tropical cyclone. The results of Experiments 2–5 are discussed in sections 5–7, and those of Experiments 6 and 7 in section 8.

As a broad means for making quantitative comparisons of the various experiments, Table 2 gives details of the maximum updraught and downdraught strengths at selected heights for all experiments and Table 3 lists the corresponding maximum and minimum vertical vorticity in these experiments.

4. Control experiment

Experiment 1 has a uniform background wind of $10\,\mathrm{m\,s^{-1}}$ above the boundary layer, and no background rotation (Table 1). The principal features of updraught evolution are as follows.

4.1. Vertical velocity

The maximum updraught and downdraught strengths, $w_{\max}$ and $w_{\min}$, are 25.8 and $10.5\,\mathrm{m\,s^{-1}}$, respectively (Table 2). As the updraught rises, the vertical velocity maximum occurs at progressively larger heights and longer times: in particular, the maximum at heights of 2, 5 and 9 km occurs at 24, 28 and 40 min, respectively. In contrast, the downdraught maximum at a height of 2 km occurs at 40 min.

Figure 4 shows horizontal cross-sections of vertical velocity at a height of 2 km for Experiment 1 at 24 and 40 min after the initial time. The earlier time is that at which the updraught velocity is a maximum at this level and the later time is when the downdraught is a maximum. These cross-sections are typical of those in the other experiments at similar stages of development. The annular region of downdraught surrounding the updraught core in Figure 4(a) is part of the subsiding branch of the upward-propagating thermal and moves upwards with the thermal. This region is separate from the low-level, rain-induced downdraught that occurs at later times.

Because of the low-level vertical shear and the fact that the wind vector veers with height, the updraught at 2 km does not remain symmetric: the subsiding branch of the rising thermal is weaker on the upper right of the cell, while stronger positive gradients of vertical velocity occur on the left (Figure 4(a), i.e. on the upwind side) of the cell where the horizontal convergence is largest (not shown). Animations of the fields indicate that the patterns of weak vertical motion beyond the subsiding branch of the thermal are gravity waves generated by the cell. At 40 min, when the downdraught at 2 km is a maximum (Figure 4(b)), the updraught at this level has all but decayed, being less than $2\,\mathrm{m\,s^{-1}}$.

Table 2. Maximum vertical velocity, $w_{N\max}$, and minimum vertical velocity, $w_{N\min}$, at a height of N km and the times at which they occur, $t(w_{N\max})$ and $t(w_{N\min})$, respectively, in Experiments 1–7. The first two columns display the maximum and minimum velocities throughout the domain and the 2 h integration time.

Experiment	$w_{\max}$	$w_{\min}$	$w_{2\max}$ ($\mathrm{m\,s^{-1}}$)	$t(w_{2\max})$ (min)	$w_{5\max}$ ($\mathrm{m\,s^{-1}}$)	$t(w_{5\max})$ (min)	$w_{9\max}$ ($\mathrm{m\,s^{-1}}$)	$t(w_{9\max})$ (min)	$w_{2\min}$ ($\mathrm{m\,s^{-1}}$)	$t(w_{2\min})$ (min)
1	25.8	−10.5	9.6	24	25.8	28	4.9	40	−5.9	40
2	25.7	−10.7	9.7	24	25.7	28	6.6	42	−7.1	40
3	28.4	−11.7	10.4	22	24.3	26	8.9	34	−5.3	22
4	25.9	−9.7	8.2	28	25.9	32	5.5	50	−4.4	34
5	25.2	−11.2	9.8	24	24.0	28	6.4	46	−4.8	38
6	18.5	−4.5	5.9	32	18.5	40	6.3	54	−2.2	52
7	19.1	−4.2	6.0	34	19.1	40	6.4	54	−1.9	32

Table 3. Maximum of the vertical component of relative vorticity, $\zeta_{N\max}$, at heights N of 500 m, 1 km and 4 km and the times at which they occur, $t(\zeta_{N\max})$, in Experiments 1–7. Shown also is the minimum of this vorticity component at heights of 1 and 4 km, together with the times at which they occur.

Experiment	$\zeta_{\max}$ ($10^{-3}\,\mathrm{s^{-1}}$)	$z(\zeta_{\max})$ (k)m	$\zeta_{0.5\max}$ ($10^{-3}\,\mathrm{s^{-1}}$)	$t(\zeta_{0.5\max})$ (min)	$\zeta_{1\max}$ ($10^{-3}\,\mathrm{s^{-1}}$)	$t(\zeta_{1\max})$ (min)	$\zeta_{4\max}$ ($10^{-3}\,\mathrm{s^{-1}}$)	$t(\zeta_{4\max})$ (min)	$\zeta_{1\min}$ ($10^{-3}\,\mathrm{s^{-1}}$)	$t(\zeta_{1\min})$ (min)	$\zeta_{4\min}$ ($10^{-3}\,\mathrm{s^{-1}}$)	$t(\zeta_{4\min})$ (min)
1	32.2	2.5	14.9	20	16.3	22	30.1	28	−13.1	24	−22.1	28
2	33.1	4.0	14.9	20	16.1	22	33.1	28	−13.0	22	−21.1	28
3	22.7	1.5	12.8	18	18.8	22	16.1	34	−13.1	18	−16.8	32
4	24.7	2.5	15.5	18	13.6	38	19.5	32	−9.4	22	−21.6	32
5	35.5	2.5	24.4	20	22.3	24	24.5	28	−10.6	22	−20.3	28
6	31.5	0.0	17.1	18	10.3	32	12.0	42	−7.2	28	−9.3	40
7	31.7	0.0	16.3	18	9.3	34	11.7	40	−7.4	28	−8.0	44

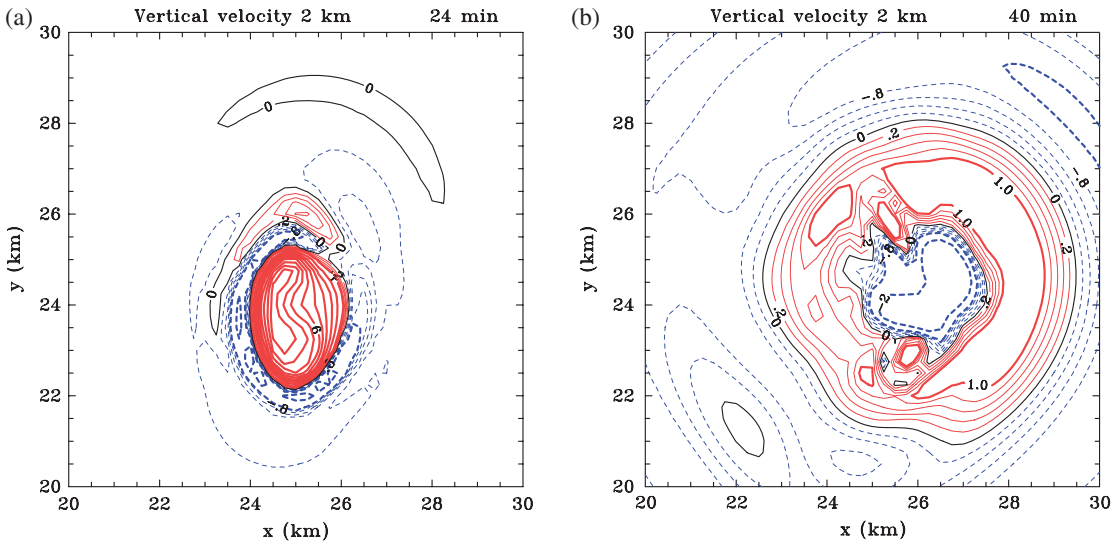

Figure 4. Horizontal cross-sections of the vertical velocity at a height of 2 km in Experiment 1 at (a) 24 min and (b) 40 min. Contour interval: thin contours 0.2–0.8 m s^{-1}; thick contours 1 m s^{-1}. Solid (red) contours positive, dashed (blue) contours negative. The thin black curve shows the zero contour.

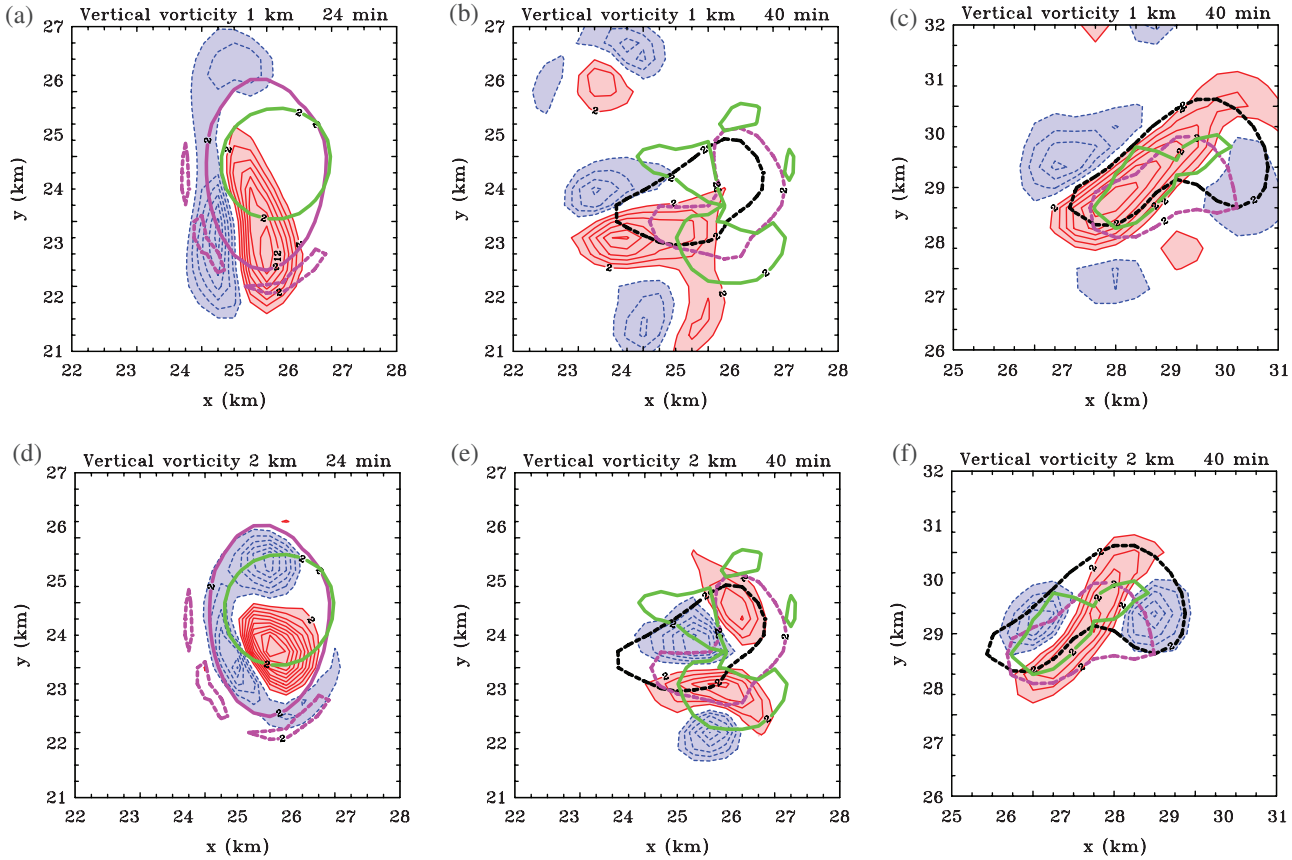

Figure 5. Horizontal cross-section of the vertical vorticity at heights of 1 and 2 km in Experiment 1 (a, b, d, e) and Experiment 5 (c, f) at chosen times. Contour interval: 2 × 10^{-3} s^{-1}. Solid (red) contours are positive, dashed (blue) contours negative. Regions of vertical vorticity are shaded (red) positive and (blue) negative. The thick solid contours show the 2 m s^{-1} vertical velocity at heights of 2 km (pink) and 4 km (green) and the thick dashed contour shows the −2 m s^{-1} vertical velocity at heights of 1 km (black) and 2 km (pink).

The downdraught falls directly into the updraught centre, which accelerates the decay of the updraught at this level.

4.2. *Vertical vorticity*

4.2.1. *Vorticity structure*

The left and middle columns of Figure 5 show horizontal cross-sections of the vertical component of relative vorticity in Experiment 1 at heights of 1 km (panels (a) and (b)) and 2 km (panels (d) and (e)) at 24 and 40 min. Regions of ascent exceeding 2 m s^{-1} at heights of 2 and 4 km and regions of subsidence with magnitude exceeding 2 m s^{-1} at heights of 1 and 2 km are shown also. At 24 min, the vorticity dipole at a height of 1 km is elongated in the south–north[†] direction, as is the vertically tilted updraught above this level. The axis of the dipole (the line joining the location of the maximum and minimum vorticity) at 1 km has an orientation close to west–east, while the background horizontal vorticity at this height is orientated closer to south–north (see Figure 2).

[†]While the orientation of the coordinate axes has no particular significance in these calculations, to aid our description we will assume that y points northwards and x eastwards.

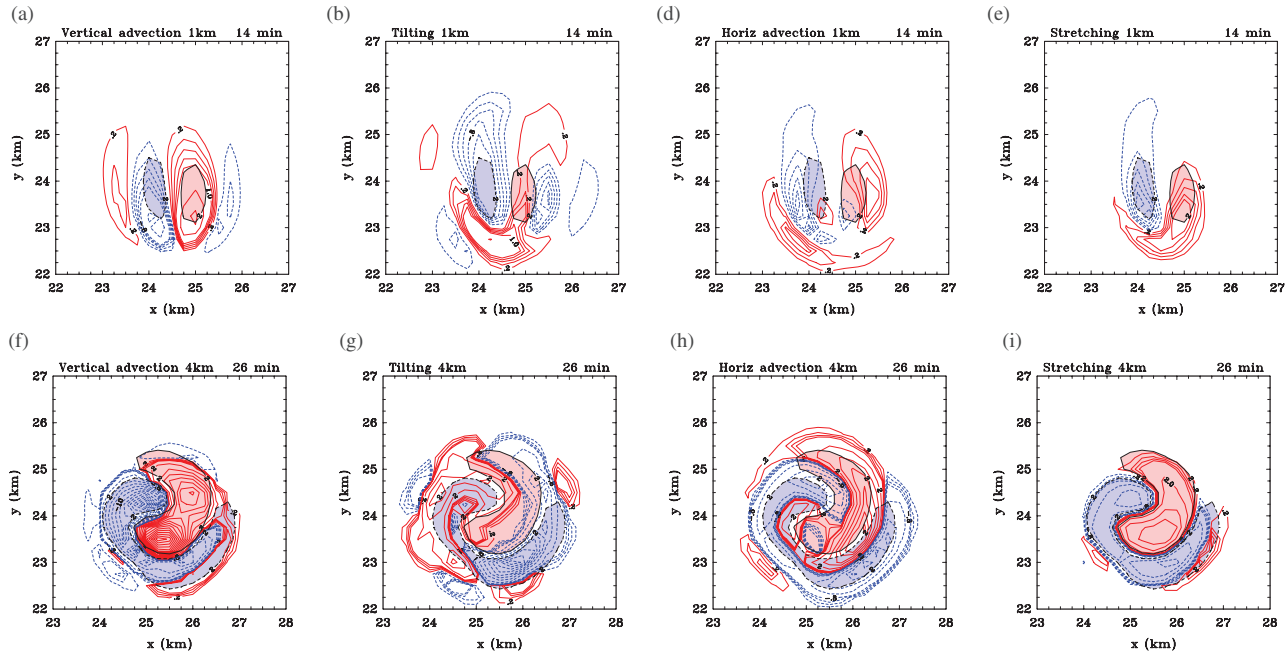

Figure 6. Vorticity tendencies at 14 min at a height of 1 km and at 26 min at a height of 4 km for Experiment 1. Contour interval: thin contours $2-8 \times 10^{-6}$ s^{-2}; thick contours 1×10^{-5} s^{-2} in upper panels (a)–(d), 4×10^{-5} s^{-2} in lower panels (e)–(h). Solid (red) contours are positive, dashed (blue) contours negative. The shaded regions enclosed by the black contour show the 2×10^{-3} s^{-1} positive (solid contour and red shading) and negative (dashed contour and blue shading) vertical vorticity.

As will be shown in the next subsection, the pattern of vertical vorticity at 24 min at a height of 1 km is dominated by the lifting and tilting of initially horizontal vortex lines *from levels near 200 m* by the updraught, where these vortex lines are orientated approximately west–east (Figure 2). At this time, the vorticity dipole at a height of 2 km has an orientation closer to north–south, while a weaker anticyclonic vorticity anomaly remains to the southwest of the cyclonic anomaly. Animations of the vorticity fields show that the anticyclonic anomaly to the southwest is an extension of the dipole that is present at 1 km and is associated with the lifting and tilting of vortex lines from this level, while the anticyclonic anomaly to the north has formed from the lifting and tilting of horizontal vorticity from heights between 1 and 2 km, where the background horizontal vorticity has a more south–north orientation. These interpretations are supported by an analysis of contributions to the vorticity tendency shown below.

At 40 min, three dipoles are evident at a height of 1 km, while only two are present at 2 km (Figure 5(b) and (e)). This complex vorticity pattern is a result of the remnant vorticity produced by the updraught, together with new dipole patterns resulting from the downward displacement and tilting of vortex lines by the downdraught. Of course, stretching of vorticity will enhance the local vorticity anomalies and compression will diminish their magnitude.[‡] Because of the complexity of the vorticity patterns at later times, it is hard to see how they might generalize to other situations. Nevertheless, these complexities would have implications for understanding the aggregation of convectively induced vorticity anomalies during vortex evolution (Nguyen *et al.*, 2008; Deng *et al.*, 2012). They may have implications also for the conceptual model for eyewall contraction proposed by Hogsett and Stewart (2014).

4.2.2. *Vorticity tendencies*

In support of the interpretations of the vertical vorticity structures given above, we present now an analysis of the contributions of various terms in the tendency equation for vertical vorticity, ζ. This equation may be written in the form

$$\frac{\partial \zeta}{\partial t} = -\mathbf{u}_\mathrm{h} \cdot \nabla_\mathrm{h}(\zeta + f) - w\frac{\partial \zeta}{\partial z} + \frac{\zeta + f}{\rho}\frac{\partial \rho w}{\partial z} + \left(\frac{\partial w}{\partial y}\frac{\partial u}{\partial z} - \frac{\partial w}{\partial x}\frac{\partial v}{\partial z}\right) + \frac{1}{\rho^2}\left(\frac{\partial \rho}{\partial x}\frac{\partial p}{\partial y} - \frac{\partial \rho}{\partial y}\frac{\partial p}{\partial x}\right), \quad (3)$$

where ρ is the density, (u, v, w) are the velocity components in the rectangular coordinate system (x, y, z), $\mathbf{u}_\mathrm{h} = (u, v, 0)$ is the horizontal velocity vector and ∇_h is the horizontal gradient operator. The five terms on the right-hand-side of Eq. (3) represent the horizontal advection of ζ, the vertical advection of ζ, the amplification of absolute vorticity by stretching, the tilting of horizontal vorticity into the vertical and the solenoidal generation of ζ, respectively.

Figure 6 shows the first four vorticity tendency terms at a height of 1 km at 14 min and 4 km at 26 min, times at which the updraught is a maximum at these levels (the solenoidal term simply produces toroidal vorticity as a result of the cloud buoyancy). At a height of 1 km, the main contribution to the vorticity tendency is from the vertical advection term, which has a dipole pattern similar to that of the vertical vorticity itself at this time. In contrast, the tilting term is weaker in magnitude and has a dipole pattern oriented approximately north–south, reflecting the orientation of background horizontal vorticity at this level (Figure 2). The vorticity tendency from horizontal advection is much weaker in magnitude than the other terms, whereas the stretching term is comparable in magnitude to the tilting term. The pattern of the stretching term is similar to the sum of the vertical advection and tilting terms, as these are the main terms generating vorticity at this height and time. As vertical vorticity is generated, stretching acts to strengthen it.

At 2 km height (not shown), the vertical advection term is dominant also, at least initially. As a result, at early times the structure of the vertical vorticity dipole at this level reflects that at levels below 2 km. However, as the vertical velocity approaches its maximum at 2 km, the other tendency terms become appreciable also and lead to a clockwise rotation of the dipole so that its axis is oriented north–south.

At 4 km height, the tendency terms (the bottom panels of Figure 6) are particularly interesting, because this level

[‡]The stretching and thereby amplification of ambient (or system-scale) vorticity by convection by itself does not lead to an increase in the circulation around a *fixed* loop embedded in the flow, because stretching leads to a contraction in the areal extent of the loop (see Haynes and McIntyre, 1987; Raymond *et al.*, 2014).

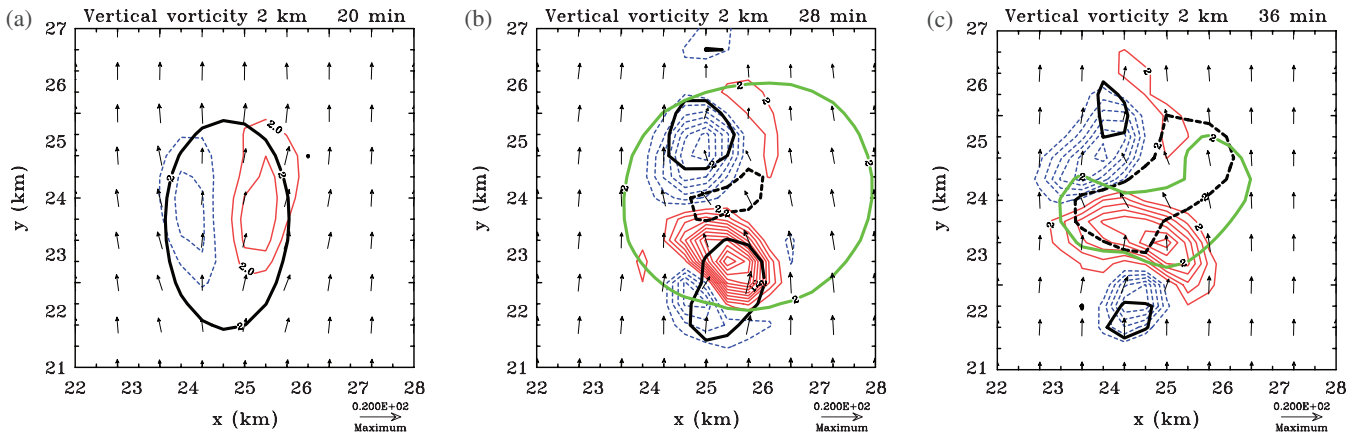

Figure 7. Horizontal cross-sections of vertical vorticity for Experiment 1 at a height of 2 km at: (a) 20 min, (b) 28 min and (c) 36 min. Contour interval: vertical vorticity contours $2 \times 10^{-3}\,\mathrm{s}^{-1}$. Solid (red) contours are positive, dashed (blue) contours negative. Vertical velocity: thick contour $2\,\mathrm{m\,s}^{-1}$, solid (black) contour positive, dashed (black) contour negative. The thick solid shaded (green) contour shows the $2\,\mathrm{m\,s}^{-1}$ vertical velocity at a height 4 km. Wind vectors are relative to the maximum vector at the bottom right of the plot. The uniform flow that was added to the wind profile to keep the convection near the centre of the computational domain is removed from these wind vectors, so that in the far field these vectors correspond with the original flow.

is well above the height at which there is any background horizontal vorticity to be tilted. Nevertheless, the maximum ζ is $3.1 \times 10^{-2}\,\mathrm{s}^{-1}$, which is only marginally smaller than the absolute maximum that occurs at a height of 2.5 km (Table 3). Again, the vertical advection tendency term is the dominant one, whereupon its structure is similar to that of ζ at 4 km. Despite the absence of background horizontal vorticity at this level, the tilting tendency is non-negligible and must be associated with the tilting into the vertical of both toroidal vorticity generated by the updraught buoyancy (represented by the solenoidal term in Eq. (3)) and horizontal vorticity advected from lower levels by the updraught. The structure of the stretching term is such as to enhance the magnitude of the dipole, while that of the horizontal advection term is to rotate the dipole clockwise and to shear it horizontally. Note that the linear theory of vertical vorticity generation presented by Rotunno (1981) and Rotunno and Klemp (1982) cannot be invoked to explain the structure of the vertical vorticity at levels where there is no background vertical shear.

4.2.3. *Vertical vorticity extrema*

Details of the maximum and minimum vertical vorticity at selected heights for Experiment 1 are included in Table 3. In this experiment, the overall maximum is $\zeta_{\max} = 3.2 \times 10^{-2}\,\mathrm{s}^{-1}$ and occurs at a height of 2.5 km. The maximum vorticity occurs at a relatively low altitude compared with those in the KSW experiments on account of the absence of background horizontal vorticity above a height of 2 km. With the standard wind profile, there is no background vertical shear and therefore no ambient horizontal vorticity to be tilted at these levels. The maximum vorticity at a height of 1 km, $\zeta_{1\max}$, is $1.6 \times 10^{-2}\,\mathrm{s}^{-1}$, while the minimum vorticity at this height, $\zeta_{1\min}$, is $-1.3 \times 10^{-2}\,\mathrm{s}^{-1}$. The difference between the magnitude of $\zeta_{1\max}$ and $\zeta_{1\min}$ is due to the clockwise-turning hodograph, which, as noted above, favours the cyclonic member of the vorticity dipole. The magnitude of the cyclonic vorticity at a height of 4 km, $\zeta_{4\max}$, is larger also than that of the anticyclonic vorticity, $\zeta_{4\min}$, which has values of 3.0 and $-2.2 \times 10^{-2}\,\mathrm{s}^{-1}$, respectively.

Recall that all experiments here have a background wind hodograph that turns clockwise with height. As found by Klemp and Wilhelmson (1978), this turning results in the cyclonic member of the vorticity dipole becoming the dominant one. An explanation for this result was given by Rotunno and Klemp (1982). They showed that, in the presence of vertical shear, dynamic pressure perturbations are induced with a high-pressure anomaly forming on the upshear side of the updraught and a low-pressure anomaly forming on the downshear side. If the shear vector does not change direction with height, these pressure anomalies will be stacked vertically, whereas when the shear vector rotates clockwise with height so does the induced pressure anomaly dipole. When the induced pressure anomaly dipole rotates clockwise with height, a favourable vertical pressure gradient is created to enhance the updraught in the region of the cyclonic vertical vorticity anomaly, i.e. cyclonic vorticity and updraught production are positively correlated. A stronger updraught located above the cyclonic vorticity anomaly leads to an increase in cyclonic vorticity production by tilting and stretching.

4.2.4. *Tendency for updraught splitting*

Figure 7 shows the evolution of the vorticity dipole at a height of 2 km in Experiment 1 from 20 to 36 min. The orientation of the dipole rotates clockwise with time from a west–east orientation at 20 min to a north–south orientation at 28 and 36 min. The background flow at this height is southerly and at lower levels it has an easterly component (Figure 2). At 28 min, there is a split of the updraught at a height of 2 km, with two distinct updraught cores, one over each member of the vorticity dipole. These two cores are separated by a downdraught, which falls through the middle of the vorticity dipole. The split is not seen at higher levels, as shown by the thick (yellow) vertical velocity contour at a height of 4 km. By 36 min, the split updraughts have all but decayed and the downdraught has grown in horizontal extent. An updraught remains at a height of 4 km, although it is smaller in horizontal extent than 8 min earlier. Although the sounding used here is based on one of the most unstable found during the PREDICT experiment, it was not sufficiently unstable for subsequent convection to be triggered along the cold-pool outflow boundary, thereby precluding the formation of a classic supercell storm.

Figure 8 shows vertical cross-sections of vertical velocity in the x–z and y–z planes through the location of $w_{\max}$ (panels (a) and (b)). It shows also vertical cross-sections of vertical vorticity in the y–z plane through the location of maximum relative vorticity at a height of 2 km (panel (c)). Panels (a) and (b) show a relatively asymmetric cell with the updraught maximum located near a height of 4 km. The strongest downdraught at this time occurs in an annular region around the updraught core at a height of about 4 km. This downdraught is part of the subsiding branch of the upward-propagating thermal. The effects of the vertical wind shear in tilting the updraught with height are most evident in the y–z plane.

The developing cell split can be seen in the y–z plane and occurs as water loading in the core of the cell begins to decelerate the updraught at mid-levels and to induce a downdraught at

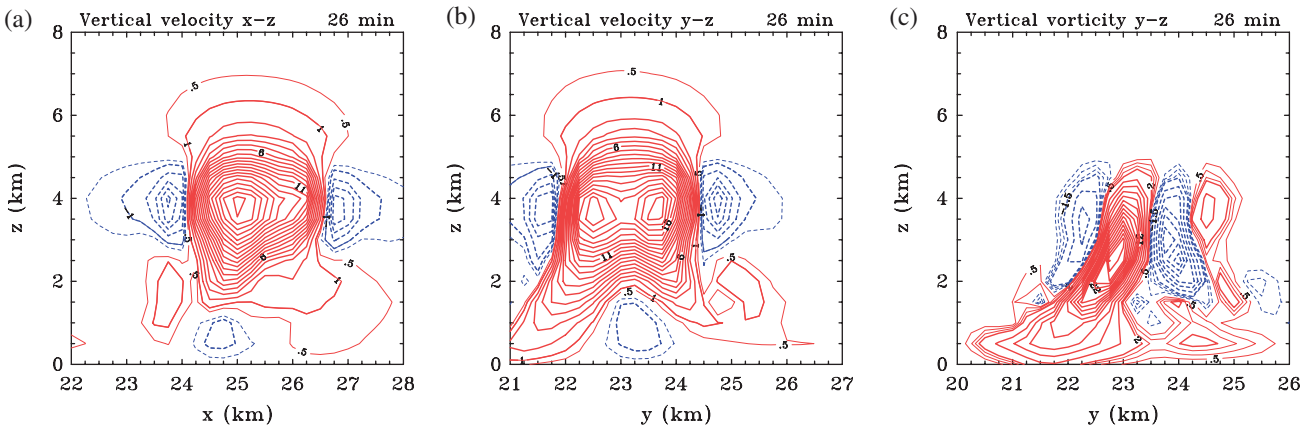

Figure 8. Panels (a) and (b) show vertical cross-sections (x–z and y–z) of vertical velocity through the centre of the domain w_{max} at 26 min for Experiment 1. Panel (c) shows a vertical cross-section (y–z) of vertical vorticity through the centre of the $\zeta_{2\,max}$ at 26 min for Experiment 1. Contour interval: vertical velocity thin contour 0.5 m s^{-1}; thick contours 1 m s^{-1}; vertical vorticity thin contours 5×10^{-4} s^{-1} to 1.5×10^{-3} s^{-1} and thick contours 2×10^{-3} s^{-1}. Solid (red) contours are positive, dashed (blue) contours negative.

low levels (Figure 8(b)). The 2 km horizontal cross-section of vertical velocity at a later time (Figure 4(b)) shows also that the downdraught falls directly beneath the updraught, while weak ascent remains in a ring around the downdraught. In this connection it is worth recalling that the development of water loading in the updraught and the subsequent formation of a downdraught is not an essential requirement for storm splitting, but it accelerates the splitting process (Rotunno and Klemp, 1985).

The vorticity structure in the y–z cross-sections (Figure 8(c)) shows an inner dipole structure with cyclonic vorticity to the left and anticyclonic vorticity to the right, embedded in a weaker dipole structure outside it with cyclonic vorticity to the right and anticyclonic vorticity to the left. To understand this structure, we note that the buoyancy of the rising thermal creates toroidal vorticity, which, together with the ambient horizontal vorticity, is tilted by the horizontal gradient of vertical velocity and further processed. Interestingly, in Figure 8(c), there is only very weak anticyclonic vorticity located below a height of about 1.7 km, in comparison with the relatively large cyclonic anomaly. This feature is evident also in a parallel slice through the vertical vorticity minimum (not shown). Rotunno (1981) shows similar results where the low-level cyclonic vorticity is dominant. He attributes this dominance to vortex stretching, which is most prominent at low levels. As the clockwise-turning hodograph favours cyclonic vertical vorticity production by vortex line tilting, the stretching term then enhances the low-level cyclonic vertical vorticity anomaly more than the anticyclonic one. Over time both dipole anomalies diminish in strength due to vortex-line compression by the downdraught, but the stronger cyclonic anomaly persists at later times.

4.2.5. *Vorticity maximum evolution*

Figure 9 shows time–height cross-sections of the maximum and minimum vertical vorticity and vertical velocity in Experiment 1 (these quantities may not occur at the same horizontal location). Note that significant vertical vorticity is generated up to a height of about 10 km (panel (a)), even though there is no horizontal vorticity above a height of 2 km and no background vertical vorticity at all. Thus, the vertical advection and tilting of vortex lines originating in the boundary layer have a significant effect through a large depth of the troposphere. The maximum cyclonic and anticyclonic vorticity occurs between 2 and 4 km and persists longest within this height range. Time–height cross-sections of maximum and minimum vertical velocity for Experiment 1 are shown in Figure 9(c) and (d). The convective cell decays in less

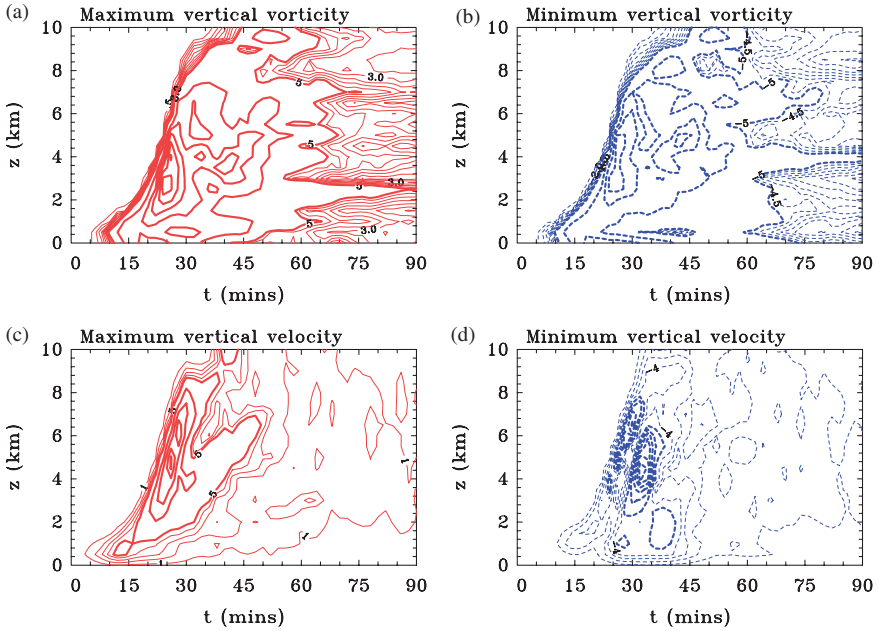

Figure 9. Time–height series of (a) maximum vertical vorticity, (b) minimum vertical vorticity, (c) maximum vertical velocity and (d) minimum vertical velocity in Experiment 1. Contour intervals: vertical vorticity thin contours 0.5–4.5 $\times$ 10^{-3} s^{-1}, thick contours 5×10^{-3} s^{-1}; vertical velocity thin contours 1 m s^{-1}, thick contours 5 m s^{-1}.

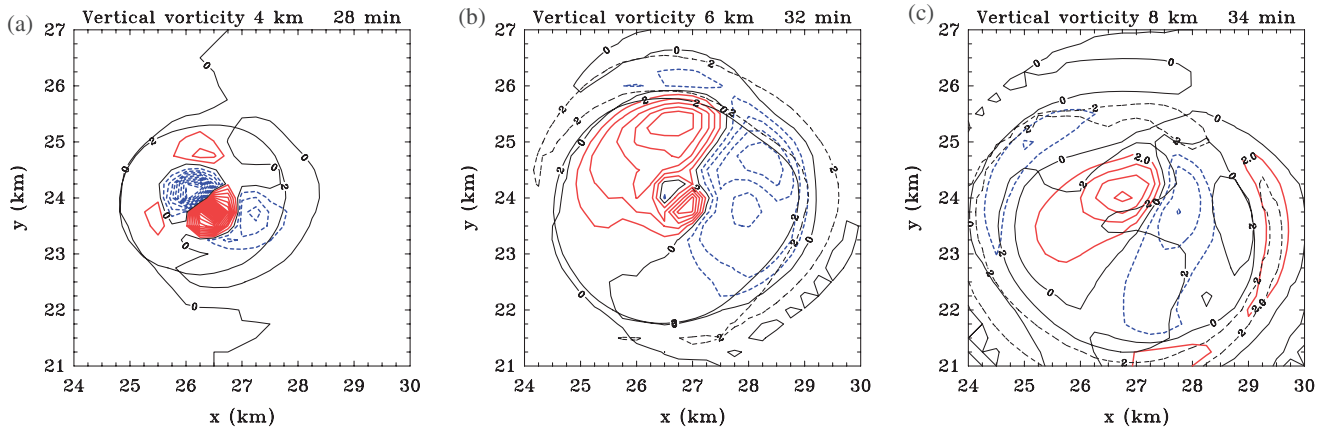

Figure 10. Horizontal cross-section of the vertical vorticity at various heights in Experiment 2 at (a) 28 min, (b) 32 min and (c) 34 min. Contour interval: 2×10^{-3} s^{-1}. Solid (red) contours are positive, dashed (blue) contours negative. The thin black curve shows the zero contour. The thick black solid contour show the 2 m s^{-1} vertical velocity and the thick black dashed contour shows the -2 m s^{-1} vertical velocity. The time chosen in each panel is 2 min after the maximum vertical velocity is found at that height.

than an hour (as happens in all the experiments) and the vertical vorticity anomalies persist at later times, consistent with the findings of Wissmeier and Smith (2011).

4.2.6. *Section summary*

In summary, the rising convective cell develops a dipole structure of vertical vorticity by lifting and tilting horizontally oriented background vortex lines into the vertical. The dipole forms first near the surface and has a west–east orientation. Subsequently, as the rising thermal breaks through a particular height, the orientation of the vorticity dipole is a result of the vertical advection of vertical vorticity. For example, at a height of 1 km, the horizontal vortex lines have a more south–north orientation so that the tilting tendency at this height has a south–north orientated dipole structure, but the vertical vorticity dipole that develops at early times has a west–east orientation. Stretching plays a role in strengthening the cyclonic vorticity at all levels where the vertical gradient of the mass flux remains positive. Because of the clockwise-turning hodograph and associated horizontal vorticity vector below 2 km, the cyclonic vorticity maximum is generally stronger in magnitude than the anticyclonic vorticity minimum and the vorticity dipole rotates clockwise with height.

In the absence of vertical shear above a height of 2 km, there is no background horizontal vorticity to be tilted. However, significant magnitudes of vertical vorticity are found up to a height of 10 km and this vorticity is associated with the vertical advection of vortex lines from the boundary layer by the updraught.

5. Negative vertical shear above the boundary layer

Experiment 1 was designed to isolate the effects of boundary-layer shear, but of course the assumption of no shear above the boundary layer is not particularly realistic. For this reason, Experiment 2 is a repeat of Experiment 1 with a negative vertical wind shear profile for the meridional wind component above a height of 2 km. Below this height, the wind profile is identical to that used in Experiment 1. Experiment 2 is an extension of Experiments 2 and 3 in KSW, which both have a low-level layer of positive vertical wind shear underlying an upper layer of negative vertical shear, but in KSW the shear was everywhere unidirectional. The additional complexity of a clockwise-turning hodograph in the boundary layer is investigated in this study.

The main differences between Experiments 1 and 2 lie in the vorticity structure above the boundary layer on account of the additional tilting of background vorticity by the updraught. Moreover, because the horizontal vorticity changes sign at a height of 2 km, the sign of the vertical vorticity dipole ultimately reverses with height. These features are illustrated in Figure 10, which shows horizontal cross-sections of the vertical component of relative vorticity in Experiment 2 at various times and heights above the boundary layer where the background vertical shear is negative. Plots of the vorticity patterns in the boundary layer are not shown here, as they are identical to those shown above for Experiment 1. The vertical vorticity dipole reverses in sign between heights of 4 and 6 km. Other aspects of the two calculations are similar, such as the values of the quantities given in Tables 2 and 3. Because of the additional vorticity generation by tilting above 2 km, the maximum and minimum vertical vorticity values at upper levels are larger in Experiment 2 than in Experiment 1 (for example, the maximum vorticity at a height of 8 km is twice as large in Experiment 2).

This change in sign of the vorticity dipole was found by KSW in experiments similar to Experiment 2, but where the shear was everywhere unidirectional. The main difference between Experiment 2 and those in KSW is the clockwise-turning hodograph in the boundary layer, a feature that leads to a stronger cyclonic vorticity anomaly at low levels. Although the sign of the ambient vertical shear in all these experiments reverses at a height of 2 km, the vertical vorticity dipole does not reverse in sign until a height of a little over 4 km because of the vertical advection of vertical vorticity in the updraught. This feature was not discussed by KSW. For example, at 32 min at a height of 4 km (Figure 10(a)), the corresponding vertical advection term is dominant (not shown), even though a vertical vorticity dipole opposite in sign is being generated by the tilting of the ambient horizontal vorticity at this time and height. The height to which the vertical vorticity dipole extends may be an important consideration in interpreting the merger of convectively induced cyclonic vorticity anomalies.

6. Stronger and weaker background flow

Experiments 3 and 4 are designed to examine the quantitative differences in the convectively generated vertical vorticity for a range of tropical depression strengths, from a weak incipient vortex to one close to gale force strength, focusing on the differences in vertical shear in the boundary layer. These experiments are repeats of Experiment 1 with different values of V_a (5 m s^{-1} in Experiment 3 and 15 m s^{-1} in Experiment 4, compared with 10 m s^{-1} in Experiment 1: see Table 1). Thus Experiment 3 has weaker low-level vertical shear than in Experiment 1, while Experiment 4 has stronger vertical shear.

The magnitudes of w_{max} and w_{min} in Experiment 3 (28.4 and 11.7 m s^{-1}, respectively) are larger than in Experiment 1 (in fact

they are the largest of all the experiments performed: Table 2). This result is consistent with the findings of Rozoff (2007), Wissmeier and Smith (2011) and KSW that convective cells rising in a environment with weak vertical or horizontal shear tend to have the strongest vertical velocities. In the weakly sheared environment, the initial thermal experiences less deformation and develops more rapidly. The magnitudes of w_{max} and w_{min} in Experiment 4 are smaller than those in Experiment 3 and occur later because of the larger deformation of the initial thermal by the stronger vertical shear.

Although it has the largest w_{max} (Table 2), Experiment 3 has smaller values of ζ_{max}, $\zeta_{0.5\,max}$ and ζ_{4max} than in Experiment 1 (Table 3). The reason may be traced to the weaker vertical wind shear and associated magnitude of horizontal vorticity available to be tilted into the vertical. In Experiment 4, ζ_{max} is smaller in magnitude than in Experiment 1, but for a different reason. The larger magnitude of vertical shear in this experiment leads to a weaker low-level updraught (see Table 2), which, in turn, leads to a weaker ζ_{max} in this experiment than in Experiment 1, despite there being a larger magnitude of horizontal vorticity available to be tilted into the vertical (recall that all of the background horizontal vorticity in these experiments is located below a height of 2 km).

7. Effects of ambient rotation

Tropical depressions and tropical cyclones have elevated levels of background vertical vorticity and the stretching of this vorticity will contribute to the vorticity amplification. To quantify this contribution, we repeated Experiment 1, but on an f-plane with Coriolis parameter $f = \zeta_o$ (see section 3.2). We designate this calculation as Experiment 5.

The values of w_{max} and w_{min} in Experiments 1 and 5 are similar (Table 2) and we do not attribute much significance to their differences. The value of ζ_{max} in Experiment 5 ($3.6 \times 10^{-2}\,s^{-1}$) is a little larger than in Experiment 1 ($3.2 \times 10^{-2}\,s^{-1}$), reflecting the additional amplification of ambient vertical vorticity by stretching. As shown in KSW, the presence of ambient vertical vorticity leads to a marked increase in the vertical vorticity maximum at low levels, where the vertical gradient of updraught mass flux is largest. This is the case also in Experiment 5, where $\zeta_{0.5\,max} = 2.4 \times 10^{-2}\,s^{-1}$, compared with $1.5 \times 10^{-2}\,s^{-1}$ in Experiment 1. In contrast, the vorticity maximum at a height of 4 km, ζ_{4max}, is smaller in Experiment 5 than in Experiment 1. In both experiments there is little contribution to vorticity generation by stretching at this height, because the vertical gradient of vertical mass flux is relatively small. The magnitude of ζ_{1max} is over twice as large as the magnitude of $\zeta_{1\,min}$ at this height. The clockwise-turning hodograph and the stretching of background cyclonic vorticity at low levels both contribute to this difference.

To illustrate the additional effect of ambient rotation, we show in Figure 5(c) and (f) horizontal cross-sections of the vertical component of relative vorticity in Experiment 5 at 40 min. Plots at the earlier times are not shown, as they are practically identical to the corresponding plots shown for Experiment 1. At 40 min, the vorticity features in Experiment 5 are quite different from those in Experiment 1 (compare the middle and right columns of Figure 5). The positive vorticity anomaly at a height of 1 km is slightly stronger (compare panels (b) and (c)), while the quadrupole structure at a height of 2 km has been replaced by a tripole vorticity structure (compare panels (e) and (f) of Figure 5). The downdraught is centred on the positive vorticity anomaly in both 1 and 2 km plots for Experiment 5. As discussed in section 4.2.1, the downdraught falling into the vicinity of the initial vorticity dipole leads to a complex pattern of vertical vorticity resulting from the tilting of horizontal vorticity by the convective downdraught. In this case, a vorticity tripole emerges where a larger patch of positive vorticity is flanked by two smaller negative patches. Again, this finding may have implications for understanding the merger of convectively induced vorticity anomalies during vortex evolution.

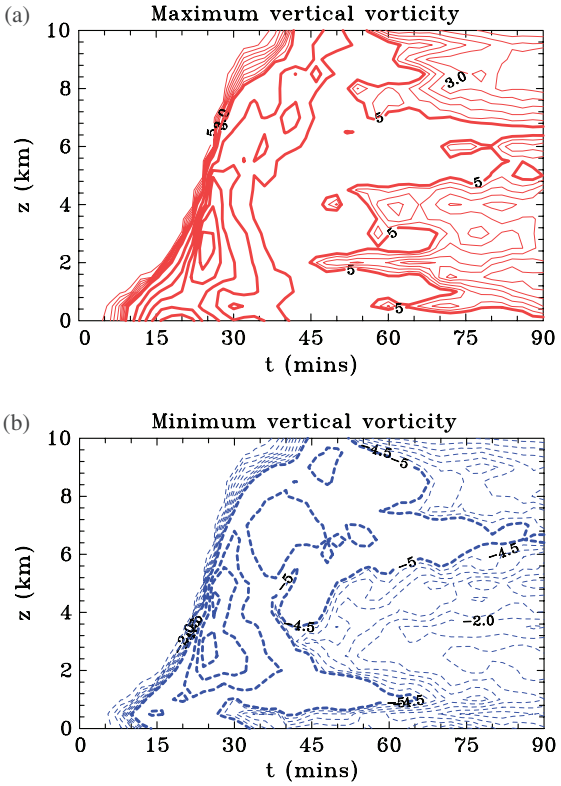

Figure 11. Time–height series of (a) maximum vertical vorticity and (b) minimum vertical vorticity in Experiment 5. Contour interval: thin contours 0.5–4.5 $\times 10^{-3}\,s^{-1}$; thick contours 5 $\times 10^{-3}\,s^{-1}$.

Figure 11 shows time–height cross-sections of the maximum and minimum vertical vorticity in Experiment 5. A feature to notice is the significant generation of vertical vorticity near the surface between 10 and 30 min in Experiment 5 (panel (a)) compared with the experiment without background rotation (Figure 9(a)). The amplified vorticity at the surface persists until 90 min. The minimum vertical vorticity decreases in magnitude at low levels when background rotation is included and this anticyclonic vorticity decays sooner than in the experiment without background rotation (compare Figures 11(b) and 9(b)).

8. Tropical cyclone boundary layer

Tropical depressions and tropical cyclones not only have elevated levels of ambient *vertical vorticity* but, because of the larger wind speeds, they provide convective environments with relatively large values of low-level *horizontal vorticity*. Examples of typical low-level wind soundings in various stages of tropical cyclone development are given in figures 7–10 of Sanger *et al.* (2014). Experiments 6 and 7 are designed to investigate the growth of convection in such environments. These experiments have a vertical wind profile characteristic of the boundary layer in the outer region of a tropical cyclone. Gale-force winds ($17\,m\,s^{-1}$) are assumed at a height of 2 km. Experiment 6 has a uniform background flow above the boundary layer, while Experiment 7 has negative uniform shear like Experiment 2, making it more realistic *vis-á-vis* tropical cyclones. Like Experiment 5, both experiments include the same value of ambient rotation.

The stronger background wind speed in these experiments is accompanied by large low-level vertical shear (see Figures 1 and 2). Further, the wind speed in Experiment 7 changes by about $6\,m\,s^{-1}$ between 2 and 8 km, which is roughly comparable to values found in an observational study of tropical cyclones. Stern and Nolan (2011) show a decline of the tangential winds of roughly $10\,m\,s^{-1}$ in such a layer. As noted earlier, large values of

vertical shear can have an appreciable effect on the strength of convective updraughts. In Experiment 6, $w_{max} = 18.5\,m\,s^{-1}$, which is $6.7\,m\,s^{-1}$ smaller than the weakest w_{max} in previous experiments. The large shear in this experiment retards the updraught development considerably, with w_{2max}, w_{5max} and w_{9max} occurring up to 14 min later than in Expt 1.

The value of ζ_{max} in Experiment 6 is comparable to that in Experiment 5 (see Table 3), but occurs closer to the surface.[§] Since the updraught at a height of 2 km is much weaker in Experiment 6 ($5.9\,m\,s^{-1}$ compared with $9.8\,m\,s^{-1}$), the larger horizontal vorticity more than compensates for the weaker updraught in the generation of vertical vorticity by tilting, since the vorticity generation by stretching must be reduced. Recall that the only difference between Experiment 6 and Experiment 5 is the larger background horizontal vorticity, especially near the surface (Figure 2). This difference would account for the fact that ζ_{max} occurs closer to the surface in Experiment 6. For example, at a height of 1 km, the magnitudes of horizontal vorticity in Experiments 5 and 6 are similar and the weaker low-level updraught in Experiment 6 leads to a much smaller value of ζ_{1max} (Table 3).

In Experiment 7, ζ_{max} is similar to that in Experiment 6 and occurs also near the surface. This result is not surprising, because both experiments have the same boundary-layer wind profile. While the updraught in Experiment 7 is slightly stronger at mid-levels than in Experiment 6, ζ_{4max} is slightly smaller. The reason is that, above 2 km, the updraught in Experiment 7 tilts ambient horizontal vorticity that has the opposite sign from that at lower levels because of the reversal of the vertical shear vector with height. This tilting acts progressively to weaken the existing vorticity dipole until its sign changes. By a height of 6 km, the vertical vorticity dipole has reversed in sign (not shown as the fields are qualitatively similar to those in Figure 10 (a) and (b)). In Experiment 7, the value of ζ_{6max} is $2.3 \times 10^{-2}\,s^{-1}$, compared with only $4.6 \times 10^{-3}\,s^{-1}$ in Experiment 6, reflecting the importance of the tilting of horizontal vorticity associated with the negative vertical shear above the boundary layer.

We examine now the applicability of the linear theory of Rotunno and Klemp (1982) to explain the vorticity structure that emerges in Experiment 6. To this end, we show horizontal cross-sections of various quantities at a height of 1 km at 16 min in Figure 12. These quantities include isopleths of the perturbation pressure, $\pm 1\,m\,s^{-1}$ contours of vertical velocity to delineate the updraught and downdraught and regions of vertical vorticity exceeding $1 \times 10^{-3}\,s^{-1}$ in magnitude. These fields are similar to those shown in Rotunno and Klemp (1982, their figure 4). As discussed earlier, these authors explained the perturbation pressure distribution in terms of linear theory, showing that high pressure forms on the upshear flank of the updraught and low pressure on the downshear flank, while vertical vorticity perturbations are aligned perpendicular to the shear vector. The shear vector at a height of 1 km in Experiment 6 points approximately west–east, so that, according to Rotunno and Klemp's theory, the vertical vorticity dipole should be aligned north–south, which is perpendicular to the shear vector. This is clearly not the case in Figure 12, indicating the importance of the vertical advection terms in the vorticity tendency equation (Eq. (3)), which are absent in the linear theory. This inference is based on the orientation of the vortex dipole at 1 km, which is aligned with the shear vector at a height of about 200–500 m. The linear theory of Rotunno and Klemp predicts also that the pressure perturbation dipole is aligned parallel to the shear vector, but this is evidently not the case, as seen in Figure 12. Clearly, the linear theory does not apply to the present flow configuration.

At this point, it is worth returning to the argument of Deng *et al.*, (2012) that the development of vortex dipoles in updraughts

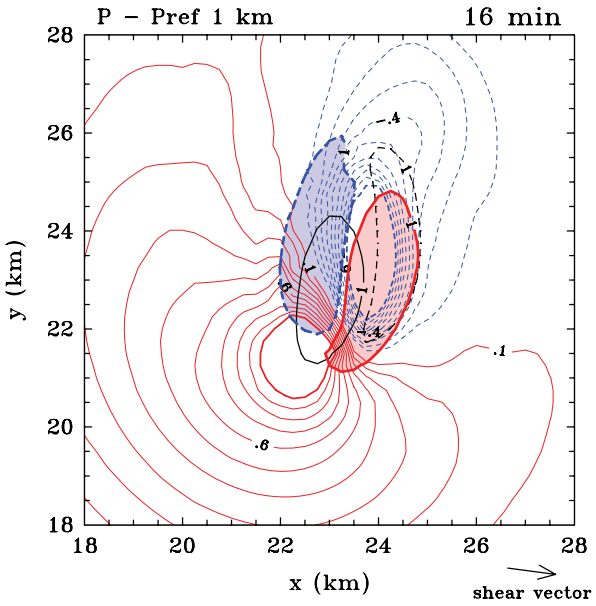

Figure 12. Perturbation pressure, vertical velocity and vertical vorticity for Experiment 6 at a height of 1 km at 16 min. The plot depicts the time when the updraught reaches this level. Perturbation pressure contours: thin contours $1–9 \times 10^{-2}$ hPa; thick contours 1×10^{-1} hPa. Solid (red) contours are positive, dashed (blue) contours negative. Vertical velocity contours: the thick black solid contour shows the $1\,m\,s^{-1}$ vertical velocity and the thick black dashed contour shows the $-1\,m\,s^{-1}$ vertical velocity. Vertical vorticity contour: the thick contour shows the $1 \times 10^{-3}\,s^{-1}$ vertical vorticity. The thick solid (red) contour is positive, the dashed (blue) contour negative. Regions of vertical vorticity are shaded (red) positive and (blue) negative. A reference vector for the vertical shear at this height is given at the bottom right of the plot.

in the presence of strong low-level vertical shear inhibits the aggregation of cloud-induced vorticity and is thereby detrimental to the formation of a larger-scale vortex. The results of our study show that, while the magnitude of the low-level vertical shear has a strong effect on vertical vorticity generation, the anticyclonic anomaly is weakened in the presence of both background rotation and a clockwise-turning hodograph. Both these features are typical of a warm core vortex boundary layer. As shown by Rotunno and Klemp (1982), the turning hodograph leads to a positive vertical perturbation pressure gradient that enhances the updraught in the region of the cyclonic vorticity anomaly. The result is that the stronger updraught strengthens the cyclonic vorticity anomaly at low levels because of stretching and tilting. The interaction of the vorticity remnants that evolve in a rotating environment with a clockwise-turning hodograph in the boundary layer and with negative vertical shear above will be the topic of a future study.

9. Storm splitting

We examine now the Hogsett and Stewart (2014) conceptual model, which seeks to explain the inward contraction of eyewall convection in tropical cyclones. The model is based on the idea that deep convection growing in the rapidly rotating environment of a tropical cyclone might have a character similar to 'supercell convection', which, in the middle latitudes, is a by-product of storm splitting. In KSW, a number of experiments were carried out to investigate storm splitting in a warm-cored vortex environment (see below). As it turns out, storm splitting does not occur in any of the present calculations, even though there are signs that the updraught is trying to divide into two at low levels.

Experiments 3 and 4 of KSW were designed to investigate storm splitting in a warm-cored vortex, the former in pure vertical shear and the latter in pure horizontal shear. Because of its effect in distorting the initial thermal, vertical wind shear was found to have a detrimental effect on the initiation of convection in those experiments for a given thermodynamic sounding. Indeed,

[§]The lowest model level at which the wind data are calculated is at a height of 60 m.

in early experiments with vertical shear and relatively stable sounding (the same sounding used in this study), convection did not occur. For that reason, Experiments 3 and 4 of KSW used a more unstable sounding to initiate convection, while the present study uses a larger thermal perturbation for this purpose (see section 3.3). The forgoing difficulty of simulating split storms is relevant to Hogsett and Stewart's conceptual model concerning left-moving split cells in the inner region of tropical cyclones. Since this region is typically one of reduced convective instability and has larger values of CIN, at least in the later stages of storm evolution and warm core development, it cannot be taken for granted that storms will undergo splitting.

A further issue concerning Hogsett and Stewart's conceptual model is that, as noted above, the vertical shear of the azimuthal-mean tangential wind in a tropical cyclone changes in sign with height near the top of the boundary layer. Even ignoring the additional complexities of the strong radial wind component in the boundary layer of a tropical cyclone, the results described in section 3 of KSW and in Experiments 2 and 7 here show that a change in sign of the vertical shear leads to a reversal in sign of the vertical vorticity dipole produced by the updraught at some height. This reversal of the sign of vorticity with height in the split cells is different from the classical updraught structure of mid-latitude storms. To our knowledge, the consequences of the change of sign of this dipole for the vorticity structure of successive updraughts in the case of a split storm have not been discussed previously in the literature. Hogsett and Stewart (2014) did acknowledge that the 'strongly sheared boundary layer is a critical complexity' that they intend to examine in a future study.

In this study, the additional complexities of the strong radial wind component in the boundary layer of a tropical cyclone are included also in the wind profile. As well as a change in sign of the vorticity dipole with height, there is a rotation of the low-level vorticity dipole with height and time. The effects of dipole rotation due to the strong radial wind component and the dipole changing in sign with height would appear to have important implications for Hogsett and Stewart's conjecture.

10. Conclusions

We have presented a series of idealized numerical model experiments to investigate aspects of deep convection in tropical depressions and tropical cyclones. Experiments were carried out to examine the effects of an Ekman-type boundary-layer wind profile on convective structure and in particular on vertical vorticity production by convection. Consistent with earlier studies, we find that deep convection that develops in a background of low-level vertical shear and cyclonic vertical vorticity leads to dipole structures of vertical relative vorticity in which the cyclonic gyre is favoured. This dipole structure extends through the lower to middle troposphere and outlives the convection that generates it. The dipole structure changes its orientation with both height and time as it tries to align itself with the local background wind shear at different levels.

At early times, as the initial thermal begins to rise, the orientation of the dipole corresponds to that of the ambient horizontal vortex lines near the surface. As time proceeds, the vorticity dipole extends vertically as vortex lines are carried upwards by the thermal. At levels where the ambient horizontal vorticity vector rotates with height, so does the axis of the vertical vorticity dipole, but to a lesser extent. The dipole continues to develop with the updraught, even at heights well above those where there is any ambient horizontal vorticity. Convection developing in a vortex boundary layer with negative unidirectional shear above the layer leads to dipole structures of vertical relative vorticity in which the sign of the dipole reverses with height.

The presence of ambient vertical vorticity leads to further amplification of low-level vorticity by stretching, especially near the surface where the vertical gradient of vertical mass flux is large. Further, the cyclonic vorticity anomaly at low levels persists longer while the anticyclonic anomaly decays sooner compared with cells developing in an environment without ambient rotation.

In a weakly sheared boundary layer environment, the initial thermal experiences less deformation and therefore develops more rapidly, with the updraught maximum occurring sooner at a given height than in experiments with larger vertical shear. Likewise, in a strongly sheared environment, the updraught maximum at a given height occurs later because of the larger deformation of the initial thermal by the stronger shear. Nevertheless, despite having the largest updraught maximum, the experiment with the weakest boundary layer shear has the smallest vertical vorticity maximum, on account of the smaller low-level horizontal vorticity available to be tilted into the vertical.

The large magnitude of low-level vertical shear in a wind profile with gale-force winds at the top of the boundary layer is detrimental to the growth of convection, weakening both the updraught and the downdraught. However, the maximum vertical vorticity generated near the surface is relatively large because of the large ambient horizontal vorticity near the surface. In contrast, the maximum vertical vorticity at a height of 1 km is much smaller than that near the surface, because of the weaker updraught and the fact that the horizontal vorticity is similar to experiments with weaker winds aloft.

Cell splitting is an essential element of Hogsett and Stewart's conceptual model to explain the inward contraction of eyewall convection in tropical cyclones. Splitting did not occur in any of the experiments performed here, although there was an indication that the updraught was trying to split at low levels. Since the inner core region of a tropical cyclone is typically one of reduced convective instability and has larger values of CIN than in the sounding used here, at least in the later stages of storm evolution and warm core development, it cannot be taken for granted that splitting will occur. The additional complexities of dipole rotation due to the strong radial wind component and the dipole changing in sign with height would appear to have important implications for the veracity of Hogsett and Stewart's conjecture.

Acknowledgements

We thank Dr George Bryan for generously making his CM1 model available to the research community. This research was supported by the German Research Council (Deutsche Forschungsgemeinschaft) under Grant No. SM30/25-1.

References

Bryan GH. 2002. 'An investigation of the convective region of numerically simulated squall lines', PhD thesis, Pennsylvania State University, Pennsylvania, PA.

Bryan GH, Fritsch JM. 2002. A benchmark simulation for moist nonhydrostatic numerical models. *Mon. Weather Rev.* **130**: 2917–2928.

Deng Q, Smith L, Majda A. 2012. Tropical cyclogenesis and vertical shear in a moist Boussinesq model. *J. Fluid Mech.* **706**: 384–412.

Dunion JP, Marron CS. 2008. A reexamination of the Jordan Mean Tropical sounding based on awareness of the Saharan air layer: Results from 2002. *J. Atmos. Sci.* **21**: 5242–5253.

Durran DR, Klemp JB. 1983. A compressible model for the simulation of moist mountain waves. *Mon. Weather Rev.* **111**: 2341–2361.

Foster IJ, Lyons TJ. 1984. Tropical cyclogenesis: A comparative study of two depressions in the northwest of Australia. *Q. J. R. Meteorol. Soc.* **110**: 105–119.

Haynes P, McIntyre ME. 1987. On the evolution of vorticity and potential vorticity in the presence of diabatic heating and frictional or other forces. *J. Atmos. Sci.* **44**: 828–841.

Hogsett W, Stewart SR. 2014. Dynamics of tropical cyclone intensification: Deep convective cyclonic 'left movers'. *J. Atmos. Sci.* **71**: 226–242.

Kilroy G, Smith RK. 2012. A numerical study of rotating convection during tropical cyclogenesis. *Q. J. R. Meteorol. Soc.* **139**: 1255–1269.

Kilroy G, Smith RK, Wissmeier U. 2014. Tropical convection: The effects of ambient vertical and horizontal vorticity. *Q. J. R. Meteorol. Soc.*, doi: 10.1002/qj.2261.

Klemp JB, Wilhelmson RB. 1978. The simulation of three-dimensional convective storm dynamics. *J. Atmos. Sci.* **35**: 1070–1096.

Molinari J, Vollaro D. 2010. Distribution of helicity, CAPE, and shear in tropical cyclones. *J. Atmos. Sci.* **67**: 274–284.

Nguyen SV, Smith RK. 2008. Tropical-cyclone intensification and predictability in three dimensions. *Q. J. R. Meteorol. Soc.* **134**: 563–582.

Ramsay HA, Doswell CA. 2005. A sensitivity study of hodograph-based methods for estimating supercell motion. *Weather and Forecasting* **20**: 954–970.

Raymond DJ, Gjorgjievska S, Sessions S, Fuchs. 2014. Tropical cyclogenesis and mid-level vorticity. *Aust. Meteorol. Oceanogr. Soc. J.* (in press).

Rotunno R. 1981. On the evolution of thunderstorm rotation. *Mon. Weather Rev.* **109**: 577–586.

Rotunno R, Klemp JB. 1982. The influence of the shear-induced pressure gradient on thunderstorm motion. *Mon. Weather Rev.* **110**: 136–151.

Rotunno R, Klemp JB. 1985. On the rotation and propagation of simulated supercell thunderstorms. *J. Atmos. Sci.* **42**: 271–292.

Rozoff CM. 2007. 'Aspects of moat formation in tropical cyclone eyewall replacement cycles', PhD thesis, Colorado State University, Fort Collins, CO.

Sanger NT, Montgomery MT, Smith RK, Bell MM. 2014. An observational study of tropical cyclone spinup in Supertyphoon *Jangmi* (2008) from 24 to 27 September. *Mon. Weather Rev.* **142**: 3–28.

Schlesinger RE. 1978. A three-dimensional numerical model of an isolated thunderstorm: Part I. Comparative experiments for variable ambient wind shear. *J. Atmos. Sci.* **35**: 690–713.

Smagorinsky J. 1963. General circulation experiments with the primitive equations I. The basic experiment. *Mon. Weather Rev.* **91**: 99–165.

Smith RK, Montgomery MT. 2012. Observations of the convective environment in developing and non-developing tropical disturbances. *Q. J. R. Meteorol. Soc.* **138**: 1721–1739.

Smith RK, Montgomery MT. 2013. On the existence of the logarithmic surface layer in the inner core of hurricanes. *Q. J. R. Meteorol. Soc.* **140**: 72–81.

Stern DP, Nolan DS. 2011. On the vertical decay rate of the maximum tangential winds in tropical cyclones. *J. Atmos. Sci.* **68**: 2073–2094.

Vogl S, Smith RK. 2009. Limitations of a linear model for the hurricane boundary layer. *Q. J. R. Meteorol. Soc.* **135**: 839–850.

Weisman ML, Klemp JB. 1984. The structure and classification of numerically simulated convective storms in directionally varying wind shears. *Mon. Weather Rev.* **112**: 2479–2498.

Wilhelmson RB, Klemp JB. 1978. A numerical study of storm splitting that leads to long-lived storms. *J. Atmos. Sci.* **35**: 1974–1986.

Wissmeier U, Smith RK. 2011. Tropical-cyclone convection: The effects of ambient vertical vorticity. *Q. J. R. Meteorol. Soc.* **137**: 845–857.

